Dual functional mesoporous silica colloidal electrolyte for lithium-oxygen batteries

Hailiang Mu [a], Xiangqun Zhuge [a], Guogang Ren [b], Kun Luo [a,*], Zhengping Ding [a], Yurong Ren [a], Zhihong Luo [c,*], Maryam Bayati [d], Ben Bin Xu [d], Xiaoteng Liu [a,d,*]

[a] Changzhou Key Laboratory of Intelligent Manufacturing and Advanced Technology for Power Battery, School of Materials Science & Engineering, Changzhou University, Changzhou 213164, PR China
[b] Department of Engineering and Technology, School of Physics, Engineering and Computer Science, University of Hertfordshire, Hatfield, Hertfordshire AL10 9AB, UK
[c] Guangxi Key Laboratory of Optical and Electronic Materials and Devices, Guilin University of Technology, Guilin 541004, PR China
[d] Department of Mechanical and Construction Engineering, Faculty of Engineering and Environment, Northumbria University, Newcastle upon Tyne NE1 8ST, UK

ARTICLE INFO

ABSTRACT

Dual functional mesoporous silica ($mSiO_2$) colloidal electrolytes are promising to protect lithium anode and accelerate the reaction kinetics on cathode for lithium-oxygen batteries (LOBs).

In this work, we achieved a significantly extended battery life (from 55 to 328 cycles) of LOB by using $mSiO_2$ with a concentration of 80 mg L^{-1} in the colloidal electrolyte, compared with the one using conventional $LiClO_4$/ DMSO electrolyte. The rate performance and full-discharge capacity are also dramatically enhanced. The as-synthesized $mSiO_2$ has a special ordered hexagonal mesoporous structure, with a high specific surface area of 1016.30 m^2/g, which can form a stable colloid after mixing with 1.0 M $LiClO_4$/DMSO. The side reactions of Li stripping/plating are suppressed, thus the cycling life performance of LOB is enhanced by relieving the attack of superoxide intermediates. The co-deposition of mesoporous $mSiO_2$ and Li_2O_2 also effectively accelerated the decomposition of the discharge product by promoting the mass transfer at the cathode. This investigation of suppressing side reactions using non-aqueous electrolytes will shed a new light on the design and development of novel lithium metal batteries.

1. Introduction

The lithium-oxygen battery (LOB) has been well-known for its prestige theoretical energy density ($\approx$ 3500 Wh kg^{-1}) among all the state-of-the-art rechargeable batteries [1–3]. However, challenges remain in various aspects, such as sluggish decomposition of lithium peroxide (Li_2O_2), quick depletion of lithium (Li) metal, electrolyte cleavage and intrinsic safety issues [4–6]. Dendritic growth [7,8] and corrosion of Li are common phenomena detrimental to the anode. Recent reports have shown some effective approaches to protect Li-ion anode by using solid electrolytes [9–11] or electrolyte additives [14,15]; Chemical/electrochemical pre-treatments [16,17] and the addition of artificial SEI layers [12,13] also improves the stability of Li anodes. For the cathode, oxygen reduction reaction (ORR) occurs during battery discharging. The oxygen is reduced to generate Li_2O_2 crystals through diffusing into the electrolytes with high donor numbers

including dimethyl sulfoxide (DMSO) and 1-methylimidazole (Me-Im) etc., and deposit on the cathode (solution pathway). There is also a surface pathway to directly react at the cathode to produce film-like Li_2O_2 in the electrolytes with low donor numbers, such as dimethyl ether (DME), tetraethylene glycol dimethyl ether (TEGDME) and acetonitrile [18]. The diffusion of ORR intermediates can also trigger the decomposition of electrolytes and the corrosion of Li anodes. The discharge product during battery charging cannot go through a complete decomposition, thus tend to accumulate if the charging potential increases and lead to failure of the LOBs because of cathode passivation [19,20], due to the low solubility of Li_2O_2 and the sluggish kinetics of oxygen evolution reaction (OER), the presence of byproducts and the poor mass transfer.

Couple of strategies have been developed to prompt the cathode reactions by preventing the deposition of the insoluble discharge product. In terms of bulk electrode modification, Peng et al. reported a

porous gold (Au) cathode that maximized the content of reversible product Li_2O_2 in ORR process, where 95 % of the initial capacity was retained after 100 cycles [21]. Ganapathy et al. introduced NiO nanoparticles to refine Li_2O_2 grains and accelerated grain decomposition to prevent cathodic passivation [22]. Hwang et al. embedded discharge product into the carbon macroscopic pores with mesoscale channels and openings connecting and found that the specific size of the pores enhanced the capacity and cyclability of the LOBs, meanwhile it inhibited the side reactions [23]. The addition of catalyst, such as noble metals (Pt, Ru), transition metal oxide (Co_3O_4, MoO_2) and transition metal-nitrogen-carbon (Fe, Co—N—C) [24–28], also improves the performance of lithium oxide battery. However, insoluble discharge product deposits on the catalyst surface cause its dysfunction. Nitrogen-doped graphene has been reported to have enhanced ORR catalytic activity while being used as cathode [29], and Au or Pd nanoparticles were attempted to decorate carbon nanotubes as active sites, to control the morphology and reduce the size of Li_2O_2 [30]. Redox mediators, i.e. LiI, tetrathiafulvalene (TTF) and 2,2,6,6-tetramethyl-piperidinyloxyl (TEMPO), were reported to assist the decomposition of discharge products and extend the cycle life of LOBs [31–33], but they were corrosive to Li anode.

Recently, the solid additives based colloidal electrolyte dispersion emerged as interesting solution [34,35], because they can absorb on the surface of discharge product (Li_2O_2), and effectively accelerate the OER kinetics with extra improvement of the electric conductivity of cathode. Additive materials include Au and Ag nanoparticles [37,38], organic molecular cage-protected Ru nanoclusters [36], and other solid additives. Kim *et al* found that the suspended Li_2O nanoparticles change the Li^+ solvation environment in aprotic electrolytes [39], and created the inorganic-rich solid-electrolyte interphases on Li anode, led to the uniform plating/stripping of Li. Mesoporous materials have been widely applied in energy storage and conversion owing to their extraordinarily high surface areas and large pore volumes [40]. Yu *et al* dispersed molecular sieve powders into the TEGDME electrolyte, where the inorganic additive adsorb superoxide (LiO_2) in the electrolyte and allow the ORR intermediate to generate Li_2O_2 by disproportionation ($LiO_{2, ad} + LiO_{2, ad} \rightarrow Li_2O_2 + O_2$). The discharge capacity of LOB significantly increased 63 times, because the formation of Li_2O_2 was converted from surface pathway to solution pathway [41].

Mesoporous silica has been a viable candidate to be used in chemical adsorption, catalytic applications and environmental remedy, due to the adjustable morphology, controllable particle size and structure, large surface area, biocompatibility, low cost, simple preparation process [42,43]. In this study, we achieve the uniform suspension of $mSiO_2$ in electrolyte and utilized it to explicitly improve the processes on both cathode and anode, therefore, lead to an enhanced performance of LOBs. The hexagonal mesoporous structure with extremely high surface area accommodates the colloid optimised stripping/plating processes, by homogenising Li^+ flux at the anode and enhancing the decomposition of by-product at the cathode. This work offers a proof of concept to suppress side reactions with mesoporous colloids and enhance the performance of LOBs, which can be potentially expanded to other lithium metal batteries.

2. Experimental

2.1. Materials and chemicals

Cetyltrimethylammonium bromide (CTAB, $\geq$ 99 %), ethanol ($\geq$99.7 %), sodium hydroxide (NaOH, $\geq$ 96.0 %) and tetraethyl orthosilicate (TEOS, $\geq$ 28.4 %) were purchased from Sinopharm Chemical Reagent Co., Ltd., China. Multiwalled carbon nanotubes (MWNTs, $\geq$ 98 %), dimethyl sulfoxide (DMSO, 99.9 %) and propylene carbonate (PC, 99.7 %) were bought from Sigma-Aldrich. Glass fiber separator (d = 18 mm, GF/D, Whatman) and carbon paper (TGP-H-060, Toray) were used directly as purchased. Lithium perchlorate (LiClO$_4$, $\geq$ 99.99 %, Sigma-

Aldrich) was dried in a vacuum oven at 120 °C for 12 h before adding into 1.0 mol/L LiClO$_4$/DMSO electrolytes. Molecular sieves (4 Å, Sigma-Aldrich) after activation were added to the electrolytes for the purpose of removing any moisture for one week prior to use. Lithium sheets (d = 14 mm, Tianjin Zhongneng Lithium Industry Co., Ltd.) are immersed in 0.1 mol/L LiClO$_4$/PC solution for at least 3 days.

2.2. Preparation of mesoporous silica (mSiO$_2$) colloidal electrolyte

0.201 g of CTAB, 10.17 g of ethanol, 128 g of deionized water and 0.1 g of NaOH were added into a round-bottomed flask, and the mixture was magnetically stirred at a rate of 600 rpm and heated in an oil bath at 30 ℃ for 30 min. Then, 1 g of TEOS was added to the mixture and kept reacting for 5 h. After standing for 24 h, the mixture was centrifugally separated, and the precipitate was collected and dried in an oven at 80 ℃. After calcinating in a muffle furnace at 550 ℃, the resultant mSiO$_2$ powder is obtained.

Different amounts of mSiO$_2$ powders were dispersed in 1.0 mol/L LiClO$_4$/DMSO electrolytes colloidal electrolytes with the mSiO$_2$ (denoted as mSiO$_2$/LiClO$_4$/DMSO) concentrations of 10 mg mL^{-1}, 30 mg mL^{-1}, 50 mg mL^{-1}, 70 mg mL^{-1}, 80 mg mL^{-1} and 100 mg mL^{-1}, respectively.

2.3. Battery assembly and testing

10 mg of MWNTs were dispersed in 20 mL of ethanol under ultra-sonication, the ink was sprayed uniformly on carbon paper with a loading of 0.1 mg cm^{-2}. After drying for 12 h in a vacuum oven at 80 °C, the carbon paper with MWNTs was cut into square (~1 cm^2) to be used as cathodes. Then, the coin cell (CR2032 with holes) was assembled following the sequence of "Li anode - glass fiber separator - injection of electrolyte - MWNTs cathode" in an argon-filled glove box (Nanjing Jiumen Automation Technology Co., Ltd., H_2O < 0.1 ppm, O_2 < 0.1 ppm). Battery testing was performed in an oxygen atmosphere ($\geq$99.9 %). The long-term cycling was carried under a current density of 1 A g^{-1} with a fixed capacity of 1000 mAh g^{-1} based on the loading amount of MWNTs, and the cut-off voltages were set up at 2.0 V and 4.5 V. The rate performance was tested with the fixed capacity of 1000 mAh g^{-1}, and current density values of 3 A g^{-1} and 5 A g^{-1} were applied. For the full-discharge test, the discharge current was set up at 0.1 mA and the cut-off voltage was 2.0 V.

Two types of symmetrical batteries were tested, stainless steel (SS| SS) and lithium plates (Li|Li) batteries. Glass fibre separators soaked with selected electrolytes and CR2032 coin cells (no holes) were used to test symmetrical batteries. The SS|SS symmetrical cell was employed to study the effect of suspending mSiO$_2$ on the ionic conductivity of electrolyte, while the Li|Li cell was used to investigate the influence of colloidal electrolyte with mSiO$_2$ on the stripping/plating of Li.

2.4. Characterizations

Field emission desktop scanning electron microscope (Phenom LE, Thermo Fisher Scientific), high-resolution transmission electron microscope (JEM-2100, JEOL) and X-ray diffractometer (XRD, D/max 2500PC, Rigaku) are utilised for morphology and structure characterisation. Raman spectrometer (532 nm, DXR2, Thermo Scientific) is used for the discharge product analysis. The adsorption–desorption isotherm was tested by a Surface Area & Porosimetry System (ASAP2460, Micromeritics). Electrochemical impedance spectroscopy (EIS) testing was carried out in the frequency range from 1 MHz to 0.1 Hz by using an Electrochemical Workstation (CHI 760E, Shanghai Chenhua Instrument Co.) with an AC amplitude of 5 mV. The ionic conductivity of electrolyte was measured in a symmetrical coin cell with two stainless steel electrodes (SS|SS) by using the following equation: $\sigma = d/R_b S$, where R_b is the solution resistance, d represents the thickness of the glass fiber separator (~890 μm), and S represents the geometric area of SS

electrodes. A rotating ring-disk electrode (RRDE-3A, ALS Co., Ltd.) equipped with a glassy carbon (GC, with an area of 0.126 cm^2) disk and a Pt ring (with an area of 0.189 cm^2) was employed to analyze the ORR catalytic activity. The GC disk electrode was modified by a pre-mixed slurry containing 4 mg of MWNTs, 100 μL of Nafion perfluorinated resin solution, 800 μL of H$_2$O and 200 μL of ethanol. The resulting GC disk electrode was covered by a layer of MWNTs at a mass loading of 0.1 mg cm^{-2}. Pt wire was used as the counter electrode, and Ag/AgNO$_3$ was used as reference electrode (the silver wire is immersed in DMSO containing 0.1 M AgNO$_3$ and calibrated in the glove box before use) [34]. The electrolyte was firstly flushed with oxygen for 30 min.

3. Results and discussion

3.1. mSiO$_2$ and colloidal electrolytes

Fig. 1a is the SEM image of as-synthesized mSiO$_2$ particles, which mainly appear in the shape of ellipsoids. Fig. S1 further shows the size distribution of mSiO$_2$ particles by the long axis length, an average size of 200 ± 10 nm (N = 120). Fig. 1b displays the high-resolution TEM image, in which the as-synthesized mSiO$_2$ particle exhibits close-packed hexagonal alignment of the pores. XRD analysis in Fig. 1c further confirms the presence of amorphous SiO$_2$ by the characteristic shoulder at around 23° [44], and the two peaks at 2° to 3° and 4° to 5° in the small-angle XRD analysis (Fig. 1d) demonstrates the hexagonal alignment of mesopores [45]. Fig. 1e displays a typical type IV isotherm in the nitrogen

adsorption/desorption test, indicative of the mesoporous structure [46,47], and the BJH model shown in Fig. 1f calculates an average pore size of ~ 3.34 nm. The BET specific surface area and pore volume are obtained as 1016.30 m^2/g and 0.73 cm^3 g^{-1}, respectively.

Fig. 1g compares the freshly prepared mSiO$_2$/LiClO$_4$/DMSO electrolyte (80 mg mL^{-1} of mSiO$_2$) and an aged electrolyte (stored for 2 months). Tyndall effect can be observed for both, where a scattering of incident lights (red) is visible because of the suspended mSiO$_2$ nanoparticles in both electrolytes. No precipitate can be found for the aged sample, indicating the colloidal electrolyte has good stability. The suspensibility of mSiO$_2$ nanoparticles in the electrolytes was examined by centrifuging at 1200 rpm for 5 min. As depicted in Fig. S3, colloidal electrolytes with different mSiO$_2$ contents in the 1.0 M LiClO$_4$/DMSO solutions have no visible change, except for the densest mSiO$_2$/LiClO$_4$/DMSO electrolyte (100 mg mL^{-1}) which precipitates are visible after centrifuging.

The ionic conductivity of mSiO$_2$/LiClO$_4$/DMSO electrolytes with different contents of mSiO$_2$ was assessed using SS|SS symmetrical cells. EIS analysis in Fig. 1h-1i indicates that the introduction of mSiO$_2$ led to a slight decrease in ionic conductivity, where the conductivity just declined from 1.39×10^{-2} S cm^{-1} (without mSiO$_2$) to 1.07×10^{-2} S cm^{-1} (with 100 mg mL^{-1} of mSiO$_2$), and therefore cannot bring with an apparent increase of internal resistance. Fig. S4 shows the electrolyte prepared using commercial solid silica (sSiO$_2$) and microporous Permutit as additive to the 1 M LiClO$_4$/DMSO. It can be seen in Fig. S4c that their ionic conductivity at a concentration of 80 mg mL^{-1} are 1.56 ×
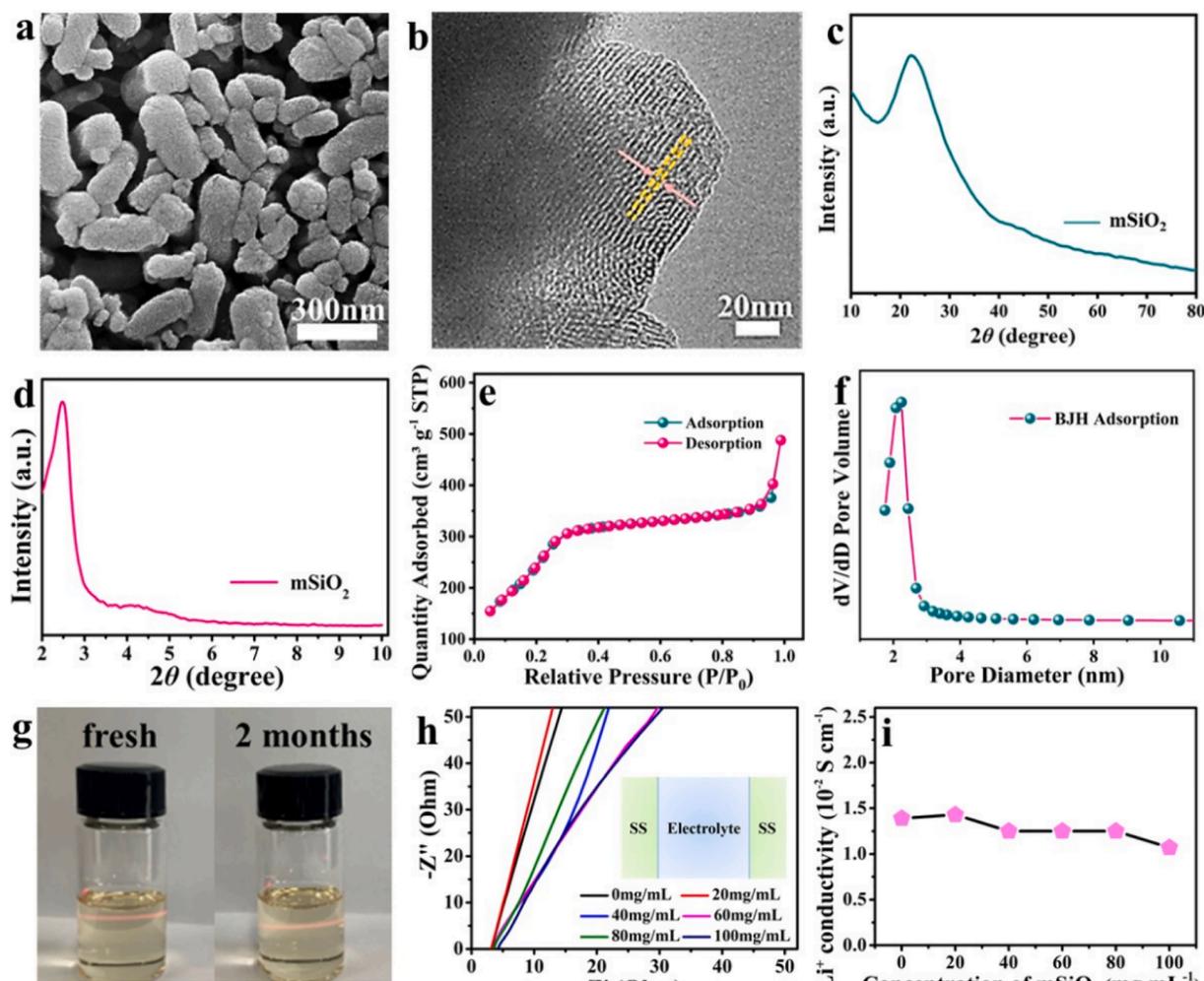

Fig. 1. (a) SEM and (b) TEM images of as-synthesized mSiO$_2$; (c) XRD analysis of mSiO$_2$, (d) small-angle XRD analysis; (e) nitrogen adsorption/desorption isotherm of mSiO$_2$; (f) BJH-adsorption model analysis; (g) Snapshots of fresh (left) and 2-month aged (right) mSiO$_2$ colloidal electrolyte; (h) EIS analysis of mSiO$_2$ colloidal electrolytes and (i) Li$^+$ conductivity vs mSiO$_2$ content.

10^{-2} S cm^{-1} (sSiO$_2$), 1.75×10^{-2} S cm^{-1} (Permutit) respectively. Meanwhile at the same concentration, the ionic conductivity of mSiO$_2$/ LiClO$_4$/DMSO electrolyte is 1.25×10^{-2} S cm^{-1} which ensures the normal operation of battery at room temperature.

3.2. LOBs with mSiO$_2$ colloidal electrolytes

Battery cycle life tests are performed to indicate the stability of electrolyte or the protective effect of mSiO$_2$ colloidal electrolyte. Fig. 2a shows the cycle number of LOB using colloidal mSiO$_2$/LiClO$_4$/DMSO electrolyte (with 80 mg mL^{-1} of mSiO$_2$) reached 328 rounds which is more than 6 times than the one using 1.0 mol/L LiClO$_4$/DMSO electrolyte (i.e., LiClO$_4$/DMSO) only, Fig. 2b shows that the LOB with 1.0 mol/L LiClO$_4$/DMSO electrolyte (i.e., LiClO$_4$/DMSO) can only operate for 55 cycles. Fig. S5a displays that the LOB with 1.0 mol/L sSiO$_2$/ LiClO$_4$/DMSO electrolyte (80 mg mL^{-1} of sSiO$_2$) can only operate for 99 cycles. Fig. S5b displays that the LOB with 1.0 mol/L Permutit/LiClO$_4$/ DMSO electrolyte (with 80 mg mL^{-1} of Permutit) can operate for 187 cycles, the existence of mesopores effectively improved the cycle performance. Fig. 2c-2d show that the cell with t colloidal mSiO$_2$/LiClO$_4$/ DMSO electrolyte has lower charge potentials and higher discharge potentials than the one with the ordinary LiClO$_4$/DMSO electrolyte, hence extending the cycle life of the LOB (the charge/discharge potential for the cell with mSiO$_2$/LiClO$_4$/DMSO electrolyte are 4.24 V/2.73 V, 4.31/2.73 V, 4.31 V/2.75 V, 4.28 V/2.76 V, 4.27 V/2.76 V, 4.28 V/2.76 V, 4.31 V/2.74 V, 4.45 V/2.66 V, 4.45 V/2.62 V for 1st, 10th, 20th, 40th, 55th, 100th, 200th, 300th, 328th cycles, respectively, the charge/ discharge potential for the cell with LiClO$_4$/DMSO electrolyte are 4.42 V/2.55 V, 4.45 V/2.72 V, 4.48 V/2.73 V, 4.49 V/2.72 V, 4.5 V/2.71 V for 1st, 10th, 20th, 40th, 55th cycles, respectively).

We also investigated the optimum mSiO$_2$ concentration, Fig. S2 shows the relationship between the concentration of mSiO$_2$ in electrolyte and the number of battery cycles. This shows that the LOB has the longest cycle life when the concentration of mSiO$_2$ is 80 mg mL^{-1} in LiClO$_4$/DMSO electrolyte. The further increase of mSiO$_2$ concentration leads to a sharp shortening of cycle life. The suspension test results in Fig. S3 confirm this finding. It can be seen that after centrifugation at 1200 rpm for 5 min, the electrolyte containing 100 mg mL^{-1} mSiO$_2$ precipitates. Table S1 shows the comparison of the cycle performance,

charge/discharge performance and full discharge performance of LOBs made of electrolytes with three different additives. mSiO$_2$/LiClO$_4$/ DMSO electrolyte shows a lower cycle life and comparable rate performance to the others, but the full discharge performance is clearly higher than the LOBs with Au/LiClO$_4$/DMSO and Ag/LiClO$_4$/DMSO electrolyte, it shows that the existence of mesoporous silica channels provides a transport channel for oxygen and Li$^+$, improves the mass transfer, avoids premature passivation of the cathode, and thus increases the capacity. Fig. 2e shows the rate performance the LOB with the LiClO$_4$/DMSO electrolyte only presents 35 and 25 cycles at the current densities of 3 A g^{-1} and 5 A g^{-1}, while the corresponding values are increased to 278 and 228 rounds for the cell with mSiO$_2$/LiClO$_4$/DMSO colloidal electrolyte, respectively, which are more than 7-fold longer than the cell with the LiClO$_4$/DMSO electrolyte at the high charge/discharge rates. Fig. S5c shows that the LOBs with sSiO$_2$/LiClO$_4$/DMSO electrolyte can only operate 49 and 36 cycles at the charge/discharge current densities of 3 A g^{-1} and 5 A g^{-1}, respectively and the LOBs with the Permutit/ LiClO$_4$/DMSO electrolyte present 91 and 60 cycles that are much lower than the LOBs with colloidal mSiO$_2$/LiClO$_4$/DMSO electrolyte.

Moreover, the full-discharge capacity for the cell with LiClO$_4$/DMSO electrolyte is tested as 4800 mAh, and the one with the mSiO$_2$/LiClO$_4$/ DMSO colloidal electrolyte reaches up to 47,600 mAh, which is one magnitude higher. The full-discharge capacity in argon atmosphere was tested for only 57 mAh as shown in the inset, suggesting that the large capacity is attributed to the ORR process. Fig. S5d further displays the full-discharge capacity of LOBs where the capacity in the LOB with sSiO$_2$/LiClO$_4$/DMSO electrolyte is tested as 8922 mAh, and the one with Permutit/ LiClO$_4$/DMSO electrolyte is 18,312 mAh. In general, the LOB with mSiO$_2$/LiClO$_4$/DMSO electrolyte shows significant improvements in battery cycle stability, rate performance, and full-discharge capacity compared to the LOBs with LiClO$_4$/DMSO, sSiO$_2$/LiClO$_4$/DMSO, and the Permutit/LiClO$_4$/DMSO electrolytes. This suggest that the colloidal electrolyte accelerates the cathode process, more discharge product is allowed to form in the cell with the colloidal electrolyte.

The characterizations of morphology and thickness of Li anodes before and after cyclability testing are performed. Fig. 3a shows a compact and smooth look of the surface of pristine Li anode, with a thickness of 323 µm (Fig. 3i). After the 1st discharge in the cell with the LiClO$_4$/DMSO electrolyte, the surface of Li anode becomes rougher as
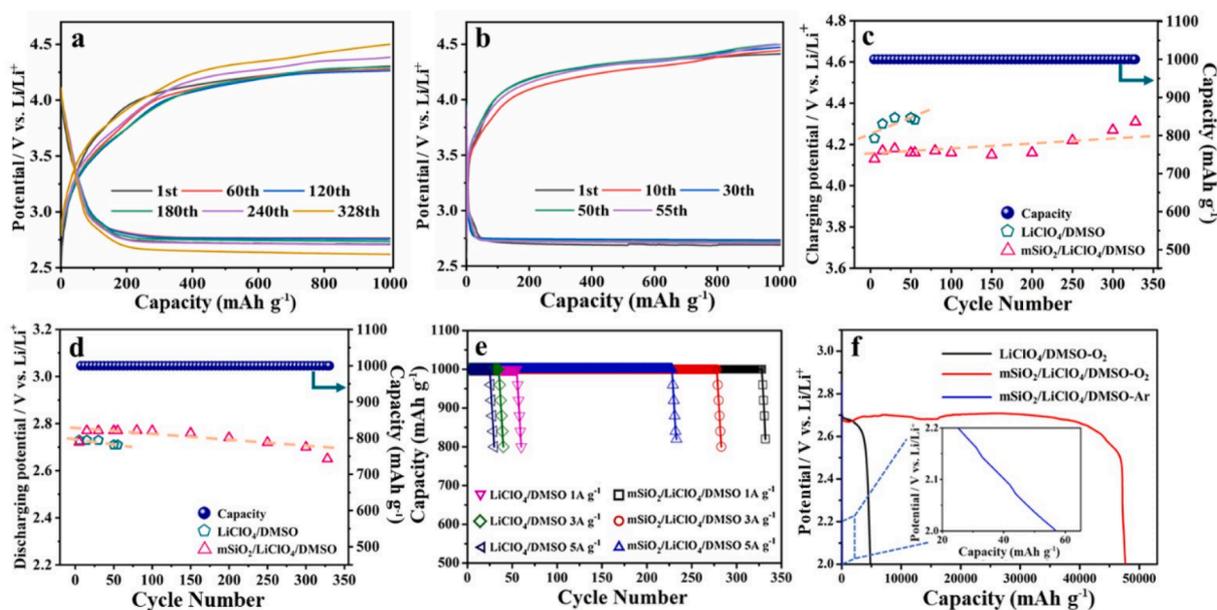

Fig. 2. Characteristics of LOBs: (a) cyclability with the mSiO$_2$/LiClO$_4$/DMSO electrolyte; (b) cyclability with the LiClO$_4$/DMSO electrolyte; (c) terminal charge potentials;(d) discharge potentials; (e)rate performance; (f) full discharge capacity, inset: enlarged curve in the mSiO$_2$/LiClO$_4$/DMSO electrolyte in argon atmosphere.
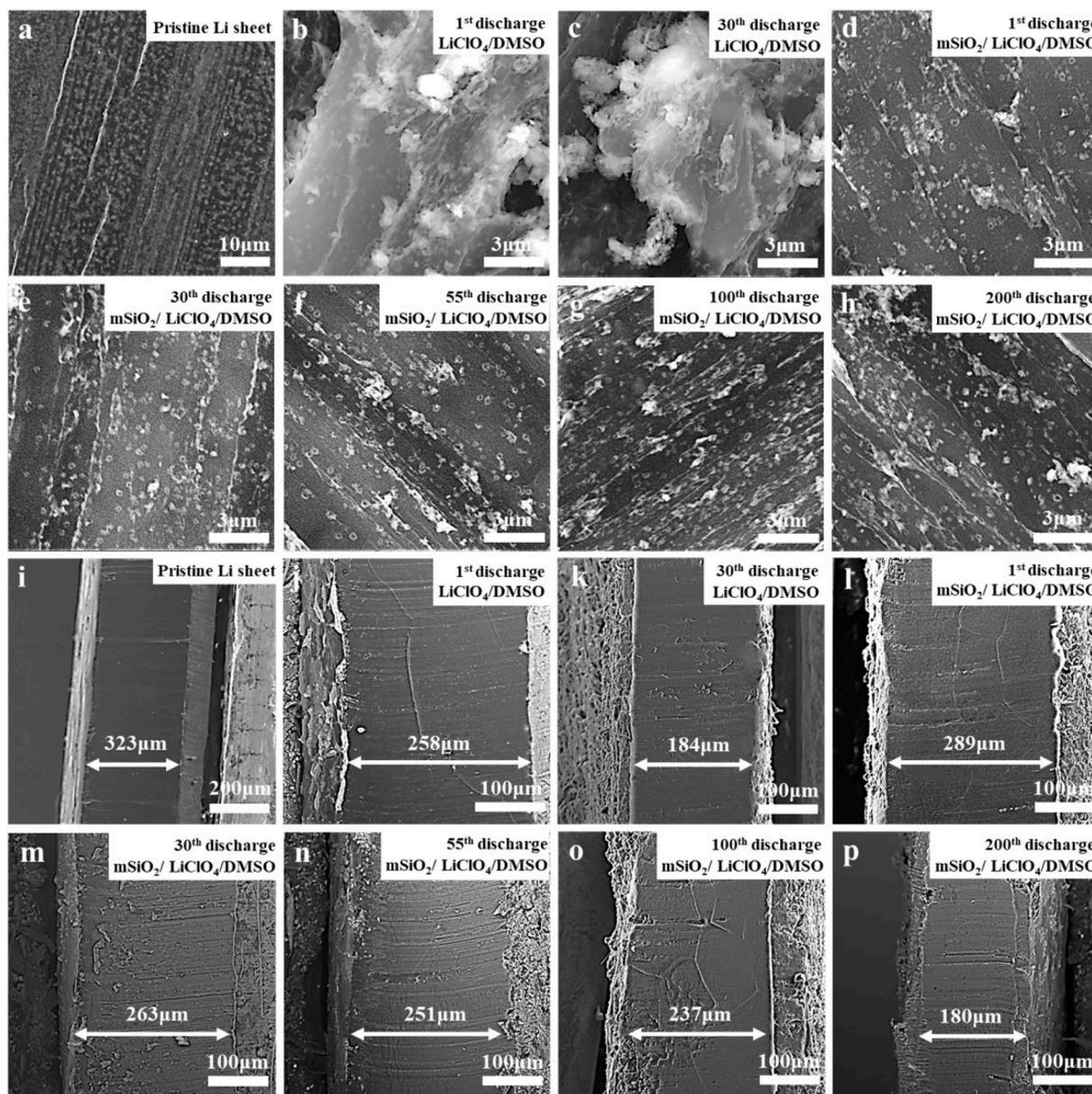
Fig. 3. Morphology and thickness of Li anodes in the LOBs: (a, i) pristine Li anode; (b, j) after the 1st discharge with the 1.0 M LiClO$_4$/DMSO electrolyte; (c, k) after the 30st discharge with the 1.0 M LiClO$_4$/DMSO electrolyte; (d, l) after the 1st discharge in the mSiO$_2$/LiClO$_4$/DMSO electrolyte (80 mg mL^{-1}); (e, m) after the 30th discharge in the cell with mSiO$_2$/LiClO$_4$/DMSO colloidal electrolyte (80 mg mL^{-1}); (f, n) after the 1st discharge in the mSiO$_2$/LiClO$_4$/DMSO electrolyte (80 mg mL^{-1}); (g, o) after the 1st discharge in the mSiO$_2$/LiClO$_4$/DMSO electrolyte (80 mg mL^{-1}); (h, p) after the 1st discharge in the mSiO$_2$/LiClO$_4$/DMSO electrolyte (80 mg mL^{-1}).

shown in Fig. 3b, its thickness is also reduced to 258 μm in Fig. 3j, After the 30th discharge in the cell with the LiClO$_4$/DMSO electrolyte, the surface of Li anode surface becomes rougher as shown in Fig. 3c, its thickness is also decreased to 184 μm in Fig. 3k. After cycling 55 times, the Li anode was totally pulverized (Fig. S6a). In contrast, the Li surface maintains rather smooth after the 1st discharge in the LOB with mSiO$_2$/ LiClO$_4$/DMSO electrolyte (Fig. 3d), and the residual Li thickness retains at 289 μm shown in Fig. 3l. Fig. 3e-h shows flat and smooth anode surface after 30, 55, 100, 200 cycles, and the thickness decreased to 263, 251, 237, 180 μm accordingly (Fig. 3m-3p). At the 328th cycle, the Li anode completely vanished (Fig. S6b). Fig. S7 compares the composition of pulverized anode powders in the LiClO$_4$/DMSO (after 55 cycles) and mSiO$_2$/LiClO$_4$/DMSO electrolytes (after 328 cycles), both assigned to LiOH according to XRD analysis. This result suggests that the mSiO$_2$ colloidal electrolyte can relieve the corrosion of Li anode, and promote the uniform stripping/plating of Li.

SEM images of LOBs is shown in Fig. 4a-h. Fig. 4a is the pristine electrode surface with MWNTs completely covered on the carbon paper substrate. Fig. 4b shows the cathode surface of LOB using LiClO$_4$/DMSO as electrolyte after 1st cycle test with undecomposed discharge product. Fig. 4c illustrates that the cathode surface is fully covered by large pieces of discharge products in the LOB with LiClO$_4$/DMSO electrolyte after cycling 55 times. Fig. 4d shows the cathode surface of the LOB with mSiO$_2$/ LiClO$_4$/DMSO electrolyte after 1st cycle, the MWNTs are clearly observed, indicating that the discharge product is decomposed. Fig. 4e-4f are images of the cathode surface of LOB with mSiO$_2$/ LiClO$_4$/DMSO electrolyte after 55 and 100 cycles. No discharge product can be observed until the one after 200 cycles in Fig. 4g. The discharge product accumulated further after 328 cycles (Fig. 4h) on the cathode, but MWNTs still appear, indicating that the suspended mSiO$_2$ in the electrolyte effectively improves the reversibility of cathode reactions.

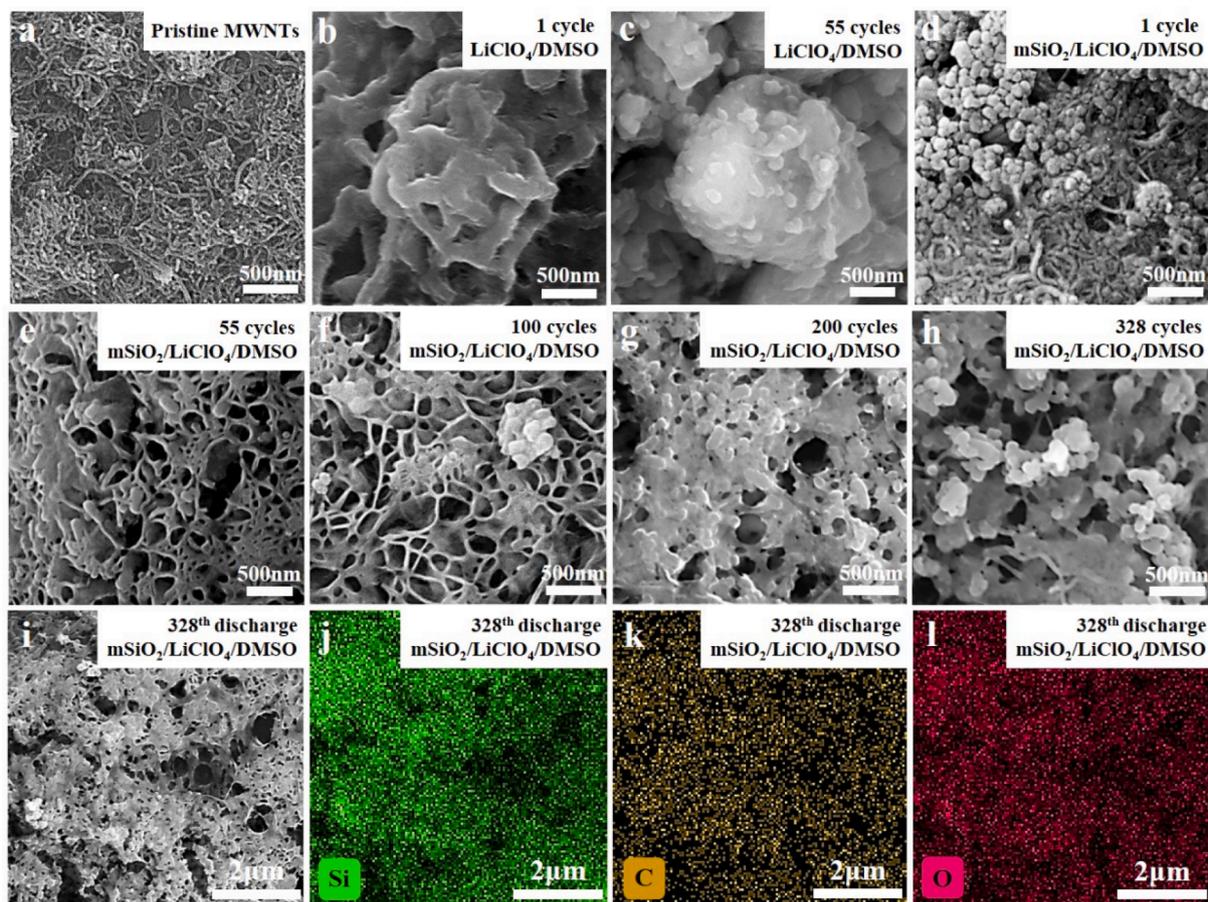Elemental mapping results (Fig. 4i-4 l) reveal Si (with C and O

Fig. 4. SEM images of the MWNTs cathodes in LOBs: (a) pristine; (b) after 1 cycle in the 1.0 M LiClO$_4$/DMSO electrolyte; (c) after 55 cycles in the 1.0 M LiClO$_4$/ DMSO electrolyte; (d) after 1 cycle in the 1.0 M mSiO$_2$/LiClO$_4$/DMSO electrolyte; (e ~ h) after 55, 100, 200, 300 and 328 cycles in the mSiO$_2$/LiClO$_4$/DMSO colloidal electrolyte; (i ~ l) element mapping of the MWNTs cathode after the 328th discharge in the mSiO$_2$/LiClO$_4$/DMSO colloidal electrolyte.

elements) in the discharge product after 328 cycles in the mSiO$_2$/ LiClO$_4$/DMSO electrolyte, indicating that the suspended mSiO$_2$ nanoparticles are co-deposited with the discharge product at the cathode. We further verify the co-deposition during the cycling of battery, The elemental mapping analysis of cathode surface with mSiO$_2$/LiClO$_4$/ DMSO colloidal electrolyte after the 1st and 55th discharges are summarized in Fig. S8 (a-d) and (e-h), with the cross-sectional elemental mapping analysis of these cathodes after the 1st, 55th and 328th discharge shown in (i-l), (m-p) and (q-t). It is concluded that the co-deposition of mSiO$_2$ and discharge products on the cathode exists in the whole cycle.

LiOH sedimentation was found on the separator material during LOBs cycling. In comparison to the pristine glass fibre separator (Fig. S9a), a minor amount of deposits can be observed after the 1st discharge (Fig. S9b) and 1st recharge (Fig. S9c) in the LOB using LiClO$_4$/ DMSO electrolyte. Most of the separator has been covered by the deposit after the 55th discharge (Fig. S9d). In contrast, sedimentation can hardly be seen on the separator after the 1st discharge (Fig. S9e) and 1st recharge (Fig. S9f) for mSiO$_2$/LiClO$_4$/DMSO electrolyte LOB, after the 55th cycle there is little can be seen (Fig. S9 g-h), even after the 100th, 150th, 200th cycles there also little can be found (Fig. S9 i-n) until the 300th cycle, some deposits can be observed (Fig. S9o) and even at the 328th cycle (Fig. S9p). In Fig. S10, XRD analysis of the deposits indicates that the composition of sediment is determined as LiOH. The colloidal electrolyte effectively suppresses the side reactions in electrolyte. The existence of mSiO$_2$ particles can promote the reversibility of positive and negative pole cycles and reduce the accumulation of by-products. Due to the existence of pores, some charge/discharge intermediates (such as

O$_2^-$, LiO$_2$) and trace water can be adsorbed, so that the side reactions caused by polarization or external environment can be reduced, enabling a long operating time for battery.

3.3. Effect of mSiO$_2$ on battery reactions

Li|Li symmetric cells were utilized to analyze the anode reactions in the LiClO$_4$/DMSO and mSiO$_2$/LiClO$_4$/DMSO electrolytes, at a current density of 0.1 mA cm^{-2} with a limited capacity of 0.1 mAh cm^{-2}. In Fig. 5a, it is found that the cell with LiClO$_4$/DMSO electrolyte (green) begins with a voltage gap of 102 mV, which rapidly expands to 939 mV after 238 h. However, the voltage gap in mSiO$_2$/LiClO$_4$/DMSO electrolyte (red) starts at 30 mV, and remains at 35 mV after 238 h. After cycling for 2300 h, the gap stays as low as 149 mV, demonstrating an improved stripping/plating of Li. This agrees with the report from Kim *et al* that the Li$^+$ solvation environment can be modified by the interaction between Li$^+$ and suspended Li$_2$O, leading to homogenised Li$^+$ flux at the Li anode [39]. Perez-Beltran *et al* also suggested that lithiation can also occur at the surface of SiO$_2$ *via* the breakage of Si-O bonds at a Li/Si ratio of 3.48 [48]. The suspended mSiO$_2$ with large specific surface area in the electrolyte can adjust the Li$^+$ flux by the interaction between mSiO$_2$ and Li$^+$, leading to the uniform plating/stripping of Li.

We next study the cathode reactions by Raman analysis. Two peaks at 670 cm^{-1} and 695 cm^{-1} are found in both products after the 1st discharge as displayed in Fig. 5b, which are assigned to the organic solvent DMSO. Besides, the spectrum in the LiClO$_4$/DMSO electrolyte (cyan line) displays two more peaks at around 485 cm^{-1} and 785 cm^{-1} assigned to LiOH and Li$_2$O$_2$ [49,50], respectively; while in the mSiO$_2$/
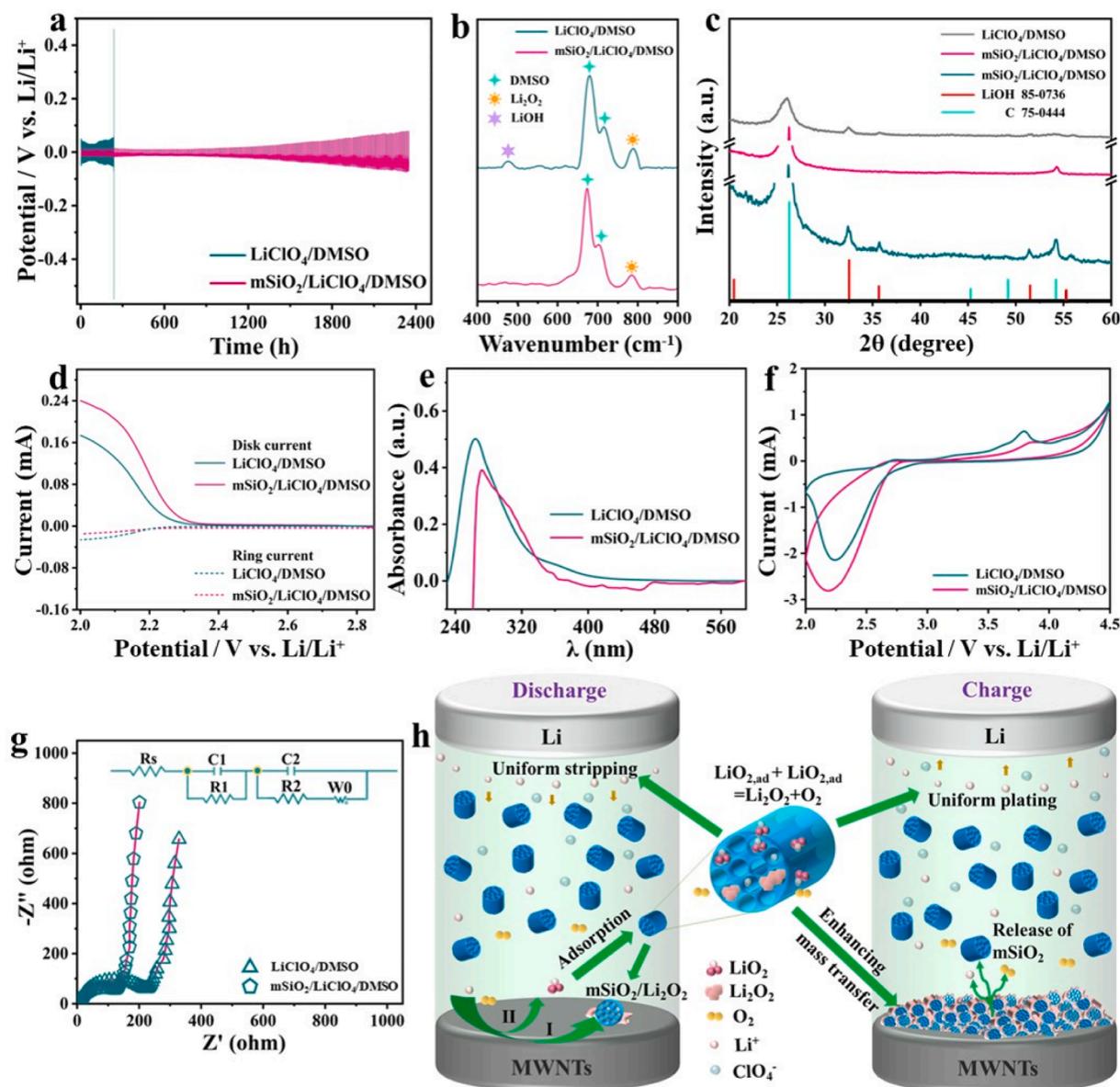
Fig. 5. LOBs with the 1.0 M LiClO$_4$/DMSO and mSiO$_2$/LiClO$_4$/DMSO (80 mg mL^{-1}) electrolytes: (a) Li|Li symmetrical cells; (b) Raman analysis of the discharge products at the 1st discharge; (c) XRD analysis of the cathode product in the LiClO$_4$/DMSO electrolyte (grey) at the 55th discharge, and the products in mSiO$_2$/LiClO$_4$/DMSO electrolyte at the 55th (pink) and 328th (blue) discharges; (d) RRDE analysis; (e) UV–vis analysis of ORR intermediates ($\lambda = 260$ nm) in the LiClO$_4$/DMSO (blue) and mSiO$_2$/LiClO$_4$/DMSO (pink) electrolytes; (f) cyclic voltammograms; (g) EIS analysis of the LOBs after the 1st discharge; (h) Illustration for the effect of suspended mSiO$_2$ in battery reaction.

LiClO$_4$/DMSO electrolyte (pink line), there is only one peak at 785 cm^{-1}, attributed to the major discharge product Li$_2$O$_2$. Fig. S11 shows the XRD analysis of discharge products in the LOBs with LiClO$_4$/DMSO (grey) at the 40th discharge and with mSiO$_2$/LiClO$_4$/DMSO at the 300th (pink) discharge, peaks of LiOH and Li$_2$O$_2$ co-exist. XRD analysis in Fig. 5c further indicates that the content of Li$_2$O$_2$ decreases with battery cycling in the LiClO$_4$/DMSO electrolyte (grey line), and the major discharge product basically becomes LiOH at the 55th discharge. In mSiO$_2$/LiClO$_4$/DMSO electrolyte (pink line), we can barely trace LiOH on the cathode at the 55th discharge, but it becomes the major product after 328 cycles (green line). The result demonstrates that the presence of mSiO$_2$ in the electrolyte is in favour of forming Li$_2$O$_2$, and therefore improves the reversibility of cathode reactions.

To understand these results, rotating ring-disc electrode (RRDE) analysis was carried out, in which the ring current associated to the oxidation of ORR intermediates (LiO$_2$ or O$_2^-$) [51], the use of Ag/AgNO$_3$ reference electrode [52]. The disk current become larger (Fig. 5d) and

the ring current is smaller in the mSiO$_2$/LiClO$_4$/DMSO electrolyte (pink lines) than those in the LiClO$_4$/DMSO electrolyte (cyan lines), showing that the content of ORR intermediates in the electrolyte is suppressed by mSiO$_2$. The contents of ORR intermediates in LiClO$_4$/DMSO and mSiO$_2$/LiClO$_4$/DMSO electrolytes (V = 10 mL) were monitored by UV–vis spectra. Fig. 5e illustrates that the absorbance at $\lambda = 260$ nm (characteristic absorbance) [53] in the mSiO$_2$/LiClO$_4$/DMSO electrolyte, which is clearly lower than the one with LiClO$_4$/DMSO electrolyte, indicative of lower content of peroxide the presence of suspended mSiO$_2$. This prove that the ORR intermediates LiO$_2$ or O$_2^-$ can be adsorbed by the suspended mSiO$_2$ when they diffuse into the electrolyte and then are converted to Li$_2$O$_2$ by disproportionation [41]. Consequently, the cleavage of electrolyte and corrosion of Li anode are inhibited.

Moreover, the significant enhancement in rate performance and full discharge capacity of LOBs closely associated with the co-deposition of mSiO$_2$ and Li$_2$O$_2$ (ref. Fig. 4i ~ 4 l). Cyclic voltammetric analysis (Fig. 5f) illustrates that the ORR peak current (cyan line) in mSiO$_2$/

LiClO₄/ DMSO electrolyte is measured as 2.81 mA, on the contrary, the one with the absence of inorganic additive (pink line) shows a result of 2.14 mA, which suggests that the incorporation with mSiO₂ improves the ORR kinetics and allows more Li₂O₂ loading at the cathode. In addition, the analysis of electrochemical impedance spectroscopy (EIS) of the LOBs after the 1st discharge also displays the apparent influence of mSiO₂ in electrolyte. In Fig. 5g, the LOB with the LiClO₄/DMSO electrolyte exhibits an impedance of 219 Ω, and the one in the mSiO₂/LiClO₄/DMSO exhibits a much smaller impedance of 121 Ω. Considering the ignorable change at anode and in electrolyte after the 1st discharge, the different impedance can be attributed to improve electric conductivity at the cathode. Fig. S12a displays the cyclic voltammograms of sSiO₂/LiClO₄/DMSO (grey line) and Permutit/LiClO₄/DMSO electrolyte (red line), the increase in ORR peak intensity further evidenced the existence of mesopores. The LOB with mSiO₂ colloidal electrolyte also exhibits a smaller impedance than the other two, as shown in Fig. S12b, the LOBs with sSiO₂/LiClO₄/DMSO (black line) and Permutit/LiClO₄/DMSO electrolyte (red line) after the 1st discharge show higher impedance values. The mesoporous structure and hydrophilic surface of mSiO₂ prompt the transfer of Li⁺ and O₂, and therefore effectively enhances the mass transfer in discharge product, lead to a reduction of electric conductivity at the cathode and the decrease of charging potentials of LOBs.

As illustrated in Fig. 5h, the suspended mSiO₂ in electrolyte enhance LOBs through three aspects: (1) *Inhibiting side reactions*. The suspended mSiO₂ can reduce the content of superoxide intermediates in the electrolyte with its large specific surface area and increases the content of Li₂O₂ in the discharge product. This prevents the electrolyte from decomposition and the Li anode from corrosion during battery cycling. The adsorption is also in favour of increasing the capacity of LOBs by enhancing the solution-growth of Li₂O₂. (2) *Improving mass transfer at the cathode*. The co-deposited mSiO₂ assists in transferring Li⁺ and O₂ by its mesopores in discharge/charge cycles and reduces the charging overpotential in the OER process. The incorporated mSiO₂ can be released into the electrolyte by decomposing Li₂O₂. (3) *Homogenising the stripping/plating of Li*. The suspended mSiO₂ in electrolyte can modify the Li⁺ solvation environment based on the interaction with Li⁺, which results in uniform Li⁺ flux and suppresses the dendritic growth of Li during cycling.

4. Conclusion

We describe an approach to achieve high performance LOBs by using a stable colloidal electrolyte containing mSiO₂ with a well-ordered hexagonal mesoporous structure (a BET specific surface area of 1016.30 m²/g). The cycle life has been extended from 55 rounds in the conventional LiClO₄/DMSO electrolyte to 328 rounds with 80 mg L⁻¹ of colloidal mSiO₂ in the electrolyte. The explicit enhancements are shown in rate performance and full-discharge capacity. Morphological and electrochemical analyses prove that the suspended mSiO₂ in the electrolyte exerts a synergistic effect on both anode and cathode. At the anode, the presence of mSiO₂ optimised the stripping/plating processes of Li by homogenising Li⁺ flux. At the cathode, the suspended mSiO₂ adsorbs the superoxide intermediates in electrolyte with its large specific surface area, and co-deposits with Li₂O₂ in discharging, thus improves the mass transfer through its mesopores for the decomposition of Li₂O₂ during charging process. Hence, the electrolyte and Li anode are protected from oxidative cleavage and corrosion, and the decomposition of Li₂O₂ was largely accelerated. We hope this approach to open a window for suppressing side reactions with mesoporous colloids in nonaqueous electrolytes, to encompass new route for future Li-ion batteries.

Declaration of Competing Interest

The authors declare the following financial interests/personal relationships which may be considered as potential competing interests:

Data availability

No data was used for the research described in the article.

Acknowledgement

Appendix A. Supplementary data

Supplementary data to this article can be found online at https://doi.org/10.1016/j.cej.2022.140761.

References

[1] J. Zhang, X. Chen, Y. Lei, H. Lu, J. Xu, S. Wang, M. Yan, F. Xiao, J. Xu, Highly rechargeable lithium oxygen batteries cathode based on boron and nitrogen co-doped holey graphene, Chem. Eng. J. 428 (2022), 131025.

[2] W. Zhang, S. Tang, Z. Chen, X. Xiong, B. Chen, K. Wu, G. Xu, S. Cheng, Y. Cao, The controllable construction of nanochannel in two-dimensional lamellar film for efficient oxygen reduction reaction and lithium-oxygen batteries, Chem. Eng. J. 430 (2022), 132489.

[3] Y.J. Oh, J.H. Kim, S.K. Park, J.S. Park, J.K. Lee, Y. Kang, Highly efficient hierarchical multiroom-structured molybdenum carbide/carbon composite microspheres grafted with nickel-nanoparticle-embedded nitrogen-doped carbon nanotubes as air electrode for lithium-oxygen batteries, Chem. Eng. J. 351 (2018) 886–896.

[4] J. Gao, X. Cai, J. Wang, M. Hou, L. Lai, L.L. Zhang, Recent progress in hierarchically structured O₂-cathodes for Li-O₂ batteries, Chem. Eng. J. 352 (2018) 972–995.

[5] M.-G. Jeong, W.-J. Kwak, J.Y. Kim, J.K. Lee, Y.-K. Sun, H.-G. Jung, Uniformly distributed reaction by 3D host-lithium composite anode for high rate capability and reversibility of Li-O2 batteries, Chem. Eng. J. 427 (2022), 130914.

[6] H. Hou, Y. Cong, Q. Zhu, Z. Geng, X. Wang, Z. Shao, X. Wu, K. Huang, S. Feng, Fluorine induced surface reconstruction of perovskite ferrite oxide as cathode catalyst for prolong-life Li-O₂ battery, Chem. Eng. J. 448 (2022), 137684.

[7] Y. Zhang, Y. Liu, J. Zhou, D. Wang, L. Tan, C. Yi, 3D cubic framework of fluoride perovskite SEI inducing uniform lithium deposition for air-stable and dendrite-free lithium metal anodes, Chem. Eng. J. 431 (2022), 134266.

[8] L. Wei, N. Deng, J. Ju, J. Kang, X. Wang, L. Ding, W. Kang, B. Cheng, A review on nanofiber materials for lithium-metal batteries to suppress the dendritic lithium growth, Chem. Eng. J. 433 (2022), 134392.

[9] B. Liu, M. Du, B. Chen, Y. Zhong, J. Zhou, F. Ye, K. Liao, W. Zhou, C. Cao, R. Cai, Z. Shao, A simple strategy that may effectively tackle the anode-electrolyte interface issues in solid-state lithium metal batteries, Chem. Eng. J. 427 (2022), 131001.

[10] K. Luo, G. Zhu, Y. Zhao, Z. Luo, X. Liu, K. Zhang, Y. Li, K. Scott, Enhanced cycling stability of Li-O₂ batteries by using a polyurethane/SiO₂/glass fiber nanocomposite separator, J. Mater. Chem. A 6 (2018) 7770.

[11] Y. Wei, H. Xu, H. Cheng, W. Guan, J. Yang, Z. Li, Y. Huang, An oxygen vacancy-rich ZnO layer on garnet electrolyte enables dendrite-free solid state lithium metal batteries, Chem. Eng. J. 433 (2022), 133665.

[12] J.-H. Kim, H.-S. Woo, W.K. Kim, K.H. Ryu, D.-W. Kim, Improved cycling performance of lithium-oxygen cells by use of a lithium electrode protected with conductive polymer and aluminum fluoride, ACS Appl. Mater. Interfaces 8 (47) (2016) 32300–32306.

[13] J. Xu, Q. Liu, Y. Yu, J. Wang, J. Yan, X. Zhang, In situ construction of stable tissue-directed/reinforced bifunctional separator/protection film on lithium anode for lithium-oxygen batteries, Adv. Mater. 27 (2017) 1606552–1606557.

[14] Z. Huang, J. Ren, W. Zhang, M. Xie, X. Li, D. Sun, Y. Shen, Y. Huang, Protecting the Li-metal anode in a Li-O₂ battery by using boric acid as an SEI-forming additive, Adv. Mater. 30 (2018) 1803270.

[15] X. Zhang, Q. Zhang, X.-G. Wang, C. Wang, Y.-N. Chen, Z. Xie, Z. Zhou, An extremely simple method for protecting lithium anodes in Li-O$_2$ batteries, Angew. Chem. Int. Ed. 57 (39) (2018) 12814–12818.

[16] M. Asadi, B. Sayahpour, P. Abbasi, A.T. Ngo, K. Karis, J.R. Jokisaari, C. Liu, B. Narayanan, M. Gerard, P. Yasaei, X. Hu, A. Mukherjee, K.C. Lau, R.S. Assary, F. K. Araghi, R.F. Klie, L.A. Curtiss, A.S.-Khojin,, A lithium-oxygen battery with a long cycle life in an air-like atmosphere, Nature 555 (2018) 502–506.

[17] Z. Luo, G. Zhu, L. Guo, F. Li, Y. Li, M. Fu, Y.-C. Cao, Y.-L. Li, K. Luo, Improving the cyclability and capacity of Li-O$_2$ batteries via low rate pre-activation, Chem. Commun. 55 (14) (2019) 2094–2097.

[18] M.T. Rauter, M. Augustin, L. Spitthoff, A.M. Svensson, Product formation during discharge: a combined modelling and experimental study for Li-O$_2$ cathodes in LiTFSI/DMSO and LiTFSI/TEGDME electrolytes, J. Appl. Electrochem. 51 (2021) 1437–1447.

[19] E. Nasybulin, W.u. Xu, M.H. Engelhard, Z. Nie, S.D. Burton, L. Cosimbescu, M. E. Gross, J.-G. Zhang, Effects of electrolyte salts on the performance of Li-O$_2$ batteries, J. Phys. Chem. C 117 (6) (2013) 2635–2645.

[20] R. Black, S.H. Oh, J.-H. Lee, T. Yim, B. Adams, L.F. Nazar, Screening for superoxide reactivity in Li-O$_2$ batteries: effect on Li$_2$O$_2$/LiOH crystallization, J. Am. Chem. Soc. 134 (6) (2012) 2902–2905.

[21] Z. Peng, S.A. Freunberger, Y. Chen, P.G. Bruce, A reversible and higher-rate Li-O$_2$ battery, Science 337 (6094) (2012) 563–566.

[22] S. Ganapathy, Z. Li, M.S. Anastasaki, S. Basak, X.-F. Miao, K. Goubitz, H. W. Zandbergen, F.M. Mulder, M. Wagemaker, Use of nano seed crystals to control peroxide morphology in a nonaqueous Li-O$_2$ battery, J. Phys. Chem. C 120 (2016) 18421–18427.

[23] C.H. Hwang, M.-J. Kwak, J.H. Jeong, K. Baek, K.-Y. Yoon, C.L. An, J.-W. Min, J. H. Kim, J. Lee, S. Kang, J.-H. Jang, J.-H. Jang, Critical void dimension of carbon frameworks to accommodate insoluble products of lithium-oxygen batteries, ACS Appl. Mater. Interfaces 14 (2022) 492–501.

[24] J. Li, Y.i. Zhao, M. Zou, ChuXin Wu, Z. Huang, L. Guan, An effective integrated design for enhanced cathodes of Ni foam-supported Pt/carbon nanotubes for Li-O$_2$ batteries, ACS Appl. Mater. Interfaces 6 (15) (2014) 12479–12485.

[25] Z. Jian, P. Liu, F. Li, P. He, X. Guo, M. Chen, H. Zhou, Core-shell-structured CNT@ RuO$_2$ composite as a high-performance cathode catalyst for rechargeable Li-O$_2$ batteries, Angew. Chem. Int. Ed. 53 (2) (2014) 442–446.

[26] C. Sun, F. Li, C. Ma, Y. Wang, Y. Ren, W. Yang, Z. Ma, J. Li, Y. Chen, Y. Kim, L. Chen, Graphene-Co$_3$O$_4$ nanocomposite as an efficient bifunctional catalyst for lithium–air batteries, J. Mater. Chem. A 2 (2014) 7188–7196.

[27] J. Liu, D. Li, Y. Wang, S. Zhang, Z. Kang, H. Xie, L. Sun, MoO$_2$ nanoparticles/ carbon textiles cathode for high performance flexible Li-O$_2$ battery, J. Energy Chem. 47 (2020) 66–71.

[28] F. Chao, B. Wang, J. Ren, Y. Lu, W. Zhang, X. Wang, L. Cheng, Y. Lou, J. Chen, Micro-meso-macroporous FeCo-N-C derived from hierarchical bimetallic FeCo-ZIFs as cathode catalysts for enhanced Li-O$_2$ batteries performance, J. Energy Chem. 35 (2019) 212–219.

[29] J. Shui, Y.i. Lin, J.W. Connell, J. Xu, X. Fan, L. Dai, Nitrogen-Doped Holey Graphene for High-Performance Rechargeable Li-O$_2$ Batteries, ACS Energy Lett. 1 (1) (2016) 260–265.

[30] X. Huang, H. Yu, H. Tan, J. Zhu, W. Zhang, C. Wang, J. Zhang, Y. Wang, Y. Lv, Z. Zeng, D. Liu, J. Ding, Q. Zhang, M. Srinivasan, P.M. Ajayan, H.H. Hng, Q. Yan, Carbon Nanotube-Encapsulated Noble Metal Nanoparticle Hybrid as a Cathode Material for Li-Oxygen Batteries, Adv. Funct. Mater. 24 (41) (2014) 6516–6523.

[31] H.D. Lim, H. Song, J. Kim, H. Gwon, Y. Bae, K.-Y. Park, J. Hong, H. Kim, T. Kim, Y. H. Kim, X. Lepró, R.O. Robles, R.H. Baughman, K. Kang, Superior Rechargeability and Efficiency of Lithium-Oxygen Batteries: Hierarchical Air Electrode Architecture Combined with a Soluble Catalyst, Angew. Chem. Int. Ed. 53 (2014) 3926–3931.

[32] Y. Chen, S.A. Freunberger, Z. Peng, O. Fontaine, P.G. Bruce, Charging a Li-O$_2$ battery using a redox mediator, Nat. Chem. 5 (6) (2013) 489–494.

[33] B.J. Bernger, A. Schürmann, K. Peppler, A. Garsuch, J. Janek, TEMPO: A Mobile Catalyst for Rechargeable Li-O$_2$ Batteries, J. Am. Chem. Soc. 136 (2014) 15054–15064.

[34] Y. Du, Y. Li, B.B. Xu, T.X. Liu, X. Liu, F. Ma, X. Gu, C. Lai, Electrolyte salts and additives regulation enables high performance aqueous zinc ion batteries: a mini review, Small 18 (43) (2022) 2104640.

[35] S. Guo, L. Qin, T. Zhang, M. Zhou, J. Zhou, G. Fang, S. Liang, Fundamentals and perspectives of electrolyte additives for aqueous zinc-ion batteries, Energy Storage Mater. 34 (2021) 545–562.

[36] L. Song, L. Zou, X. Wang, N. Luo, J. Xu, J. Yu, Realizing Formation and Decomposition of Li$_2$O$_2$ on Its Own Surface with a Highly Dispersed Catalyst for High Round-Trip Efficiency Li-O$_2$ Batteries, iScience 14 (2019) 36-46.

[37] Z. Luo, F. Li, C. Hu, D. Li, Y. Cao, K. Scott, X. Gong, K. Luo, Impact of a Gold Nanocolloid Electrolyte on Li$_2$O$_2$ Morphology and Performance of a Lithium-Oxygen Battery, ACS Appl. Mater. Interfaces 13 (3) (2021) 4062–4071.

[38] Z. Luo, F. Li, C. Hu, L. Yin, D. Li, C. Ji, X. Zhuge, K. Zhang, K. Luo, Highly dispersed silver nanoparticles for performance-enhanced lithium oxygen batteries, J. Mater. Sci. Technol. 73 (2021) 171–177.

[39] M.S. Kim, Z. Zhang, P.E. Rudnicki, Z. Yu, J. Wang, H. Wang, S.T. Oyakhire, Y. Chen, S.C. Kim, W. Zhang, D.T. Boyle, X. Kong, R. Xu, Z. Huang, W. Huang, S. F. Bent, L.-W. Wang, J. Qin, Z. Bao, Y.i. Cui, Suspension electrolyte with modified Li$^+$ solvation environment for lithium metal batteries, Nat. Mater. 21 (4) (2022) 445–454.

[40] W. Li, J. Liu, D. Zhao, Mesoporous materials for energy conversion and storage devices, Nat. Rev. Mater. 1 (2016) 16023.

[41] W. Yu, H. Wang, J. Hu, W. Yang, L. Qin, R. Liu, B. Li, D. Zhai, F. Kang, Molecular Sieve Induced Solution Growth of Li$_2$O$_2$ in the Li-O$_2$ Battery with Largely Enhanced Discharge Capacity, ACS Appl. Mater. Interfaces 10 (9) (2018) 7989–7995.

[42] Y. Ding, G.F. Yin, X.M. Liao, Z. Huang, X. Chen, Y. Yao, J. Li, A convenient route to synthesize SBA-15 rods with tunable pore length for lysozyme adsorption, Microporous Mesoporous Mater. 170 (2013) 45–51.

[43] Y. Wang, X. Du, Z. Liu, S. Shi, H. Lv, Dendritic fibrous nano-particles (DFNPs): rising stars of mesoporous materials, J. Mater. Chem. A 7 (2019) 5111–5152.

[44] R.K. Biswas, P. Khan, S. Mukherjee, A.K. Mukhopadhyay, J. Ghosh, K. Muraleedharan, Study of short range structure of amorphous Silica from PDF using Ag radiation in laboratory XRD system, RAMAN and NEXAFS, J. Non Cryst. Solids 488 (2018) 1–9.

[45] L. García-Uriostegui, H. Iván Meléndez-Ortiz, G. Toriz, E. Delgado, Post-grafting and characterization of mesoporous silica MCM-41 with a thermoresponsive polymer TEVS/ NIPAAm/ β-cyclodextrin, Mater. Lett. 196 (2017) 26–29.

[46] C.T. Kresge, M.E. Leonowicz, W.J.J. Roth, J.C. Vartuli, J.S. Beck, Ordered mesoporous molecular sieves synthesized by liquid-crystal template mechanism, Nature 359 (1992) 710–712.

[47] J.S. Beck, J.C. Vartuli, W.J. Roth, M.E. Leonowicz, C.T. Kresge, K.D. Schmitt, C.T. W. Chu, D.H. Olson, E.W. Sheppard, S.B. McCullen, J.B. Higgins, J.L. Schlenker, A new family of mesoporous molecular sieves prepared with liquid crystal templates, J. Am. Chem. Soc. 114 (27) (1992) 10834–10843.

[48] S. Perez-Beltran, G.E. Ramírez-Caballero, P.B. Balbuena, First-Principles Calculations of Lithiation of a Hydroxylated Surface of Amorphous Silicon Dioxide, J. Phys. Chem. C 119 (29) (2015) 16424–16431.

[49] L. Johnson, C. Li, Z. Liu, Y. Chen, S.A. Freunberger, P.C. Ashok, B.B. Praveen, K. Dholakia, J.-M. Tarascon, P.G. Bruce, The role of LiO$_2$ solubility in O$_2$ reduction in aprotic solvents and its consequences for Li-O$_2$ batteries, Nat. Chem. 6 (12) (2014) 1091–1099.

[50] X. Gao, Y. Chen, L. Johnson, P.G. Bruce, Promoting solution phase discharge in Li-O$_2$ batteries containing weakly solvating electrolyte solutions, Nat. Mater. 15 (2016) 882–888.

[51] Y. Zhou, Z.Y. Lyu, L. Wang, W. Dong, W. Dai, X. Cui, Z. Hao, M. Lai, W. Chen, Co$_3$O$_4$ functionalized porous carbon nanotube oxygen-cathodes to promote Li$_2$O$_2$ surface growth for improved cycling stability of Li-O$_2$ batteries, J. Mater. Chem. A 5 (2017) 25501–25508.

[52] A. Köllisch-Mirbach, I. Park, M. Hegemann, E. Thome, H. Baltruschat, Electrochemical Reduction of O$_2$ in Ca^{2+}-Containing DMSO: Role of Roughness and Single Crystal Structure, ChemSusChem 14 (2021) 2564–2575.

[53] X. Zhang, L. Guo, L. Gan, Y. Zhang, J. Wang, L.R. Johnson, P.G. Bruce, Z. Peng, LiO$_2$: Cryosynthesis and Chemical/Electrochemical Reactivities, J. Phys. Chem. Lett. 8 (2017) 2334–2338.